

THE DYNAMICS OF THE EXCITATION OF SOLAR OSCILLATIONS

LOUIS H. STROUS^{1,2,3}, PHILIP R. GOODE², AND THOMAS R. RIMMELE³

Received 1999 November 4; accepted 2000 January 20

ABSTRACT

We investigate seismic events, bursts of seismic waves that are generated locally just below the solar surface and that we detect traveling up through the photosphere. We identify a few thousand seismic events by their traveling wave character and find that they are associated with continuum darkening and downflow and have an extent of on average about 10–15 minutes and 1 Mm. Their birth rate is about $8 \times 10^{-16} \text{ m}^{-2} \text{ s}^{-1}$. The observed upwardly traveling seismic flux in the average event (as derived from velocities in the p -mode region of k - ω space) is followed after about 3 minutes by some reflected downward flux. Only a small fraction of the energy generated in the hypocenter of the event below the surface travels straight up for us to see. The bulk of the generated energy is directed or reflected downward, and is eventually transformed into p -modes. The seismic events at the surface contain about $1.5 \times 10^{19} \text{ J}$ of seismic energy each, which corresponds to an average flux level of about 8.5 kW m^{-2} over the whole surface. The total energy flow is likely more than an order of magnitude greater, and is then in the same ballpark as the estimate of Libbrecht for the power required to sustain the p -mode spectrum. We find a roughly linear relation between the peak seismic flux and the peak downward convective velocity associated with each seismic event, which does not fit the highly nonlinear relations found theoretically by Lighthill and Goldreich & Kumar for stochastic excitation by turbulent convection, but does fit the monopole source deduced by Nigam & Kosovichev from a study of the p -mode spectrum.

Subject heading: Sun: oscillations — Sun: photosphere — waves

1. INTRODUCTION

Our knowledge of terrestrial oscillations is antisymmetric with our knowledge of solar oscillations. Terrestrial oscillations are intermittent, and their source (earthquakes, generally due to release of stress between moving tectonic plates) is basically well understood. Significant oscillations can often be correlated with particular sources (earthquakes) that may have occurred on the other side of the planet. To gain more information about the mechanisms of earthquakes and the subsurface structure of the Earth, one must wait for an indeterminate period of time until another earthquake occurs.

Solar oscillations, on the other hand, are continuously being excited, and their source mechanism is not yet well established. One can measure solar oscillations at any time, but any measurement includes contributions from many source locations and times, which cannot, in general, be disentangled.

Understanding of the source of solar oscillations has been sought in two different ways. The most used method is to study global properties of the oscillations and to try to match these with particular source mechanisms. The global properties of the oscillations depend more on the characteristics of the medium they traverse than on the particulars of the source, so such studies depend on subtle effects. Lighthill (1952) investigated the generation of acoustical waves by turbulence in a homogeneous fluid. Stein (1967) and Goldreich & Kumar (1990) extended the calculations to models more applicable to the Sun. Goldreich & Kumar found support for the hypothesis that the solar

p -modes are stochastically excited by turbulent convection and that the efficiency of the conversion of convective energy into p -modes, f -modes, and propagating acoustic waves is proportional to a high power (15/2) of the velocity of energy-bearing eddies.

More recently, Chagelishvili, Tevzadze, & Goossens (1999) proposed linear conversion of convection by shear flows. Kumar & Basu (1999) compared solar p -mode velocity power spectra with synthetic spectra for various source mechanisms and found the best fits for quadrupole sources between 700 and 1050 km below the surface (top of the convection zone) and for dipole sources between 120 and 350 km deep. Nigam & Kosovichev (1999), using a similar scheme, deduce a source about $75 \pm 25 \text{ km}$ below the photosphere, with dominant monopole and secondary quadrupole contributions.

The second method is to study individual source events. On the observational side, Goode, Gough, & Kosovichev (1992) showed that the solar oscillations in their observations are excited less than 200 km below the Sun's visible surface. Rimmele et al. (1995a, 1995b) observed that the oscillations are fed by isolated seismic events that arise in the dark intergranular lanes and that the seismic flux is suppressed near magnetic field. They showed that the excitation is caused by a catastrophic cooling and collapse of the solar surface that occasionally occurs in a dark lane, and suggested that the oscillations are driven by the noise that the collapses make. Goode et al. (1998) demonstrated that the seismic events feed power to the normal modes.

On the theoretical side, Rast (1999) numerically simulated (in two dimensions) localized cooling events in the solar photosphere and studied their acoustic response, finding acoustic emission of monopolar, dipolar, and quadrupolar types in succession.

Here we elaborate on parts of the work of Rimmele et al. (1995b) and Goode et al. (1998) and elucidate the dynamical process by which the oscillations are excited. When no con-

¹ Lockheed Martin Advanced Technology Center, O/L9-41, B/252, 3251 Hanover Street, Palo Alto, CA 94304.

² Big Bear Observatory, New Jersey Institute of Technology, 40386 North Shore Boulevard, Big Bear City, CA 92314.

³ National Solar Observatory/Sacramento Peak, PO Box 62, Sunspot, NM 88349.

fusion is likely, we shall use the name *seismic event* both for the invisible subsurface and for the visible surface aspects of these collapses. Rimmele et al. (1995a, 1995b) observed the photospheric aspects of seismic events earlier, and we use their data here. Each observed seismic event is sufficiently spatially and temporally isolated that it would be rare for another to intrude on it during its 10–15 minute life. This isolation vastly simplifies efforts to understand seismic events.

2. THE DATA

A patch of quiet Sun near disk center with dimensions of roughly 60" by 50" was observed on 1994 September 5, using the Vacuum Tower Telescope (now the Richard B. Dunn Solar Telescope) of the National Solar Observatory at Sacramento Peak, New Mexico. The observations were done using a 20 mÅ passband filter consisting of the Universal Birefringent Filter and a Fabry-Perot interferometer (Bonaccini & Stauffer 1990). This combination was used to scan the profile of the magnetically insensitive ($g = 0$) Fe I $\lambda 5434$ line, yielding intensities at 13 wavelengths in the line and one wavelength in the nearby continuum. The wavelengths were selected in the following order (in mÅ relative to nominal line center): 0, +20, -20, -40, +40, +60, -60, +100, -100, +140, -140, +200, -200 and the continuum, so the line was sampled beginning near its center and then going up to higher intensities. The narrow-band filtergrams were recorded with a RCA504 CCD camera. The resolution was 0".19 by 0".25 pixel⁻¹. Exposure times were typically 150–300 ms. In addition to the narrow-band filtergrams, broadband images were recorded simultaneously with a second CCD-camera, but these broadband images were not used in the current analysis.

The line profile was scanned 122 times, yielding 122 sets of 14 filtergrams each. Each scan took 30.8 s, for a total observing time of 63 minutes. The seeing conditions varied between good and excellent during these times. The images were stabilized using a correlation tracker (Rimmele et al. 1991).

The Fe I line at 5434 Å is a well-studied and well-behaved line without blends. The results we get from this line are consistent with those obtained using different spectral lines, such as magnetically insensitive Fe I $\lambda 5576$.

3. THE DATA PROCESSING

We performed standard dark current and flat field corrections. Effects of atmospheric distortion in the white-light and filtergram images were removed using a destretching algorithm (Rimmele 1994). From the intensities as a function of wavelength we derive bisector velocities as a function of altitude (§ 3.2). From the bisector velocities we derive phases of vertically traveling waves in the p -mode region of the k - ω diagram, and then the seismic flux (the vertical wave energy flux; § 3.3). Before calculating the bisector velocities, we reduce the observations to a common time base, because otherwise the different observation times of the images at different wavelengths lead to spurious phase differences with altitude, and thence to spurious seismic flux (§ 3.1).

3.1. To a Common Time Base

Our observations were recorded one wavelength position at a time, so quantities derived directly from observations at different wavelengths, such as Doppler velocities, are based on measurements taken at different times. This leads to

spurious phase differences between observations of waves at different altitudes, which cannot easily be corrected for. We therefore reduced the observed intensities to a common time base, using Fourier interpolation (i.e., by appropriately modifying the Fourier phases while leaving the Fourier amplitudes unchanged). All observations were shifted back to the observation time of the beginning of the current wavelength cycle.

In tests with constructed random data sets with time-scales of about 3 minutes, the residual standard error left by this method is about 1% of the standard deviation of the data if the data from the whole observation period are subsequently used or about 0.1% if the first and last five time steps (154 s) are discarded. The errors decline with increasing timescale. The greater error at the beginning and end of the observation period is due to the infinite-repetition property of Fourier transforms.

3.2. To Velocities

We computed bisector velocities at intensities of 0.35 and 0.40 local continua above the local line center; these correspond to intensity levels of on average 0.54 and 0.59 times the continuum. These intensity levels sample the spectral line (as observed) near its inflection points, so they yield the greatest sensitivity of intensity to Doppler velocities. We used cubic spline interpolation to find the line-center intensity and the bisectors. We use the bisector velocities at the two intensity levels as estimates for the velocities at two different altitudes in the photosphere.

The use of bisector velocities as Doppler velocities is predicated on the assumption that a given intensity level corresponds (within reasonable limits) to the same altitude on both sides of the spectral line. Whether this assumption holds for high-resolution observations of the solar surface with convection and waves cannot be determined from remote observations alone (at least, we wouldn't know how) but could be investigated using realistic simulations of granulation, where the actual mass velocities are available for comparison with the derived bisector velocities. Such simulations now exist (e.g., Stein & Nordlund 1998), but to our knowledge they have not yet been applied to the investigation of the limitations of bisector velocities.

Our justification for the use of bisector velocities as Doppler velocities is therefore empirical. If radiative transfer effects made bisector velocities unsuitable as a proxy for wave motion, then we would expect a very strong correlation between continuum intensity and any results derived from bisector velocities—in particular, between continuum intensity and seismic flux—but our investigation found no evidence of this.

Just as for any measurement on the Sun, the value of a particular bisector velocity depends significantly on the conditions in some range of altitudes in the solar atmosphere. Because of the variation in physical conditions with space and time on the Sun, the actual altitude range that contributes significantly to a given bisector velocity varies with space and time, too, but for simple spectral lines such as the one employed by us, lower line depths correspond to lower layers as far as bisector velocities are concerned (Kučera et al. 1998; Grossmann-Doerth 1994). In model experiments, Stebbins & Marmolino (1989) found that our method faithfully detects simulated waves (similar to the ones we are looking for) traveling vertically through the photosphere. Through the bisectors, we arrive at a four-

dimensional data structure, $v(x, y, z, t)$, giving the velocity as a function of the two spatial coordinates x and y on the solar surface, the altitude z in the photosphere, and time t .

From the results of an observational investigation of formation heights from bisector velocities in our spectral line by Kučera et al. (1998), we infer average formation heights of 219 and 200 km above the $\tau_{500} = 1$ level for our bisectors. The separation is considerably less than a scale height. Selecting the levels so close together minimizes the chances of the phase difference between the levels becoming greater than 180° and therefore not uniquely determinable (see § 3.3), and minimizes the effects of variation of the physical parameters (density, sound speed) between the two altitudes. It also reduces the signal-to-noise level in the differences found between the two levels, but not so much that it becomes a problem. The results are qualitatively similar if a greater vertical separation is used.

We expanded the bisector velocity images in the y -direction (using Fourier interpolation) so that the pixel scale became equal in both directions, at $0''.19$. The field of view then measures 308 by 304 pixels.

3.3. To Seismic Flux

We calculate the seismic flux, which estimates the vertical mechanical flux in traveling waves in the p -mode region of k - ω space. Vertical waves are evanescent in the p -mode region. The p -modes themselves are very nearly standing waves that transport hardly any energy and yield hardly any seismic background. Any traveling waves that are found in the p -mode region must therefore have been generated locally and stand out well. We exclude the region of k - ω space that contains the granular signal, because granulation yields appreciable and variable signal, which may obscure locally generated seismic waves.

To isolate the seismic power, we applied a temporal frequency bandpass filter to the velocity data. The filter rejected all power below 1.35 mHz and above 6.3 mHz, and accepted all power between 2.7 and 4.95 mHz, with smooth transitions. A temporal filter is sufficient because the convective and seismic power are well separated in temporal frequency in our observations. We refer to the resulting filtered velocities as *sonic velocities*, and to the removed complement as *convective velocities*. The convective velocities show the granulation very clearly, and the sonic velocities do not.

The mechanical flux in a wave equals the product of the kinetic energy density ρV^2 (with ρ the mass density and V the wave velocity amplitude) and the group velocity v_g (Mihalas 1979). Group velocity is difficult to measure, but in the p -mode region of the k - ω diagram the group velocity is approximately related to the phase velocity v_{ph} through

$$v_g v_{ph} \approx c^2, \quad (1)$$

where c is the local sound speed.

We calculate the phase velocity from the phases obtained using the temporal Hilbert transform. The Hilbert transform, quadrature function, or associated function q is derived from the original v by shifting all phases by $+90^\circ$ in Fourier space (Bracewell 1965). By combining the original data and its Hilbert transform we can derive an instantaneous amplitude $V(t)$ and phase $\phi(t)$, from

$$v(t) = V(t) \sin \phi(t), \quad (2)$$

$$q(t) = V(t) \cos \phi(t). \quad (3)$$

Because the quadrature function is calculated using Fourier transforms, its value at a given ordinate depends on the original data at all ordinates, and it suffers from edge effects related to the infinite-repetition assumption of Fourier transforms. However, tests using overlapping time bases of different sizes show that, in our data set, such effects are noticeable only in the first few and last few frames.

Combining the preceding equations, our definition for vertical seismic flux F_{ac} for continuous data at a single fixed frequency ω is

$$F_{ac} = -\frac{\gamma P V^2}{\omega} \frac{\partial \phi}{\partial z} = -\frac{\gamma P}{\omega} \left(\frac{\partial v}{\partial z} q - \frac{\partial q}{\partial z} v \right), \quad (4)$$

where γ is the ratio of specific heats, P is the total pressure, V is the velocity amplitude, and $\partial \phi / \partial z$ is the observed velocity phase gradient with altitude. We have used that $\rho c^2 = \gamma P$. For our discrete data set we define the seismic flux as

$$F_{ac} = -\frac{\gamma P}{\omega} \frac{V_{12}^2 \Delta \phi_{12}}{\Delta z}, \quad (5)$$

where $V_{12} = (V_1 + V_2)/2$, $\Delta \phi_{12} = \phi_2 - \phi_1$, V_i is the velocity amplitude at level i , ϕ_i is the phase at level i , and $\Delta z = z_2 - z_1$ is the spanned altitude difference. In this case the phase difference can be determined only up to the nearest 360° . If one is not interested in the velocity phases and amplitudes, then an alternative definition is

$$F_{ac,2} = -\frac{\gamma P}{\omega} \frac{v_2 q_1 - v_1 q_2}{\Delta z}, \quad (6)$$

with v_i the velocity and q_i its Hilbert transform at altitude i . $F_{ac,2}$ is similar though not identical to F_{ac} , and is less computationally expensive. However, we use equation (5) because we study the phases, too.

The operational definition of seismic flux (F_{ac}) assumes a single frequency ω for all waves, and a single pressure P for both compared altitude levels. These assumptions are reasonable in our case, because (for P) the altitude difference between the compared adjacent altitude levels is considerably less than a density scale height, and because (for ω) the included range of frequencies is not very wide.

Energy fluxes such as the seismic flux are not linear functions of velocity, so cross-terms occur and the seismic flux derived from a sum of velocity components is not equal to the sum of the seismic fluxes derived from each velocity component separately. In this way, standing waves such as p -modes influence the seismic flux calculated for traveling waves, even though the seismic flux of individual p -modes is negligible. The ratio of the cross-terms flux and the traveling-waves flux is of the same order as the ratio of the corresponding velocity amplitudes. Even though it is confused by the presence of p -modes, the seismic flux is still a useful quantity. It does not generate false signals: if a significant amount of seismic flux is found somewhere, then there must be traveling waves and mechanical flux present there.

The pressure at our chosen altitude levels is $P \approx 1.0 \times 10^3$ Pa, the frequency of p -modes is about $\omega \approx 0.020$ rad s $^{-1}$, the ratio of specific heats is about $\gamma \approx 1.4$, and the altitude difference is about 19 km; from these it follows that

$$F_{ac} \approx 3.7 V_{12}^2 \Delta \phi_{12} \quad (7)$$

if the seismic flux is measured in W m^{-2} , the velocity amplitude in m s^{-1} , and the phase difference in radians.

4. MODELS

Interpretation of results is often confounded by response functions of the instruments, measurement procedures, and data reduction methods, which tend to smear out or otherwise degrade sharp features in the quantities that are being measured, and which may produce systematic results even when or where only “average” or “random” data are present. To help assess these effects in the current investigation, we constructed model velocity data sets that resemble the velocities obtained from the observations but that do not contain explicitly modeled seismic events. (Models are also indicated because the seismic flux is not a linear function of the velocities.)

The constructed data sets have the same dimensions as the data derived from the observations. Two data sets mimicking the observed velocities at the two altitude levels are constructed as follows:

1. Draw independent random values $v_1(x, t)$ and $v_2(x, t)$ from a standard normal distribution for all locations x and times t in the data volume.
2. Replace v_2 by a linear combination v'_2 of v_1 and v_2 that is still normally distributed but enforces cross-correlation coefficient c :

$$v'_2(x, t) = v_2(x, t)\sqrt{1 - c^2} + v_1(x, t)c. \quad (8)$$

3. Replace v'_2 by a version v''_2 that is shifted in time over a specified amount, using Fourier interpolation (i.e., by shifting the phase of all temporal Fourier components appropriately).

4. Replace v_1 by a version v'_1 that has the same power spectrum as the observed data at the lower altitude, by appropriately modifying the Fourier amplitudes while not modifying the Fourier phases. Likewise replace v''_2 by v'''_2 that has the same power spectrum as the observed data at the higher altitude.

The two model data sets v'_1 and v'''_2 now reflect (1) high cross-correlation between the velocity values at the two altitudes, just like the observed velocities at the selected altitude levels, (2) a time lag between the observations at the two altitudes, (3) the same spatial-temporal spectra as the observational data, and (4) no seismic events.

We can then investigate the model data in exactly the same way as the regular data and compare the results, and ascribe any differences between the data and the models to systematic effects such as seismic events. We constructed 1230 models for all combinations of one time lag out of 41 lags regularly spaced between -0.62 and $+0.62$ s, and one cross correlation out of 30 correlations regularly spaced between 0.997 and 1.000.

The model cross-correlations c cannot be directly compared with the cross-correlation found between the observational velocities at different altitudes, because the model cross-correlation is enforced before the time lag and observational power spectrum are implemented. For reference, the cross-correlation between the observational velocities at the two altitude levels is 0.9986. This value is so high because (1) p -modes are highly correlated at different altitudes, and (2) the altitude levels are close together.

The model correlation coefficient is a free parameter because it is not clear how the presence or absence of

seismic events influences the correlation between the velocities at the different altitudes.

5. SEISMIC FLUX HISTOGRAMS

The models described in § 4 lead to seismic flux distributions such as the ones displayed with the dotted and dashed curves in Figure 1. They decrease exponentially as one moves away from zero flux, with different scale fluxes for positive fluxes and for negative fluxes when the time lag is not equal to zero. In the investigated range of models, the product of the scale fluxes is approximately independent of the time lag. The distributions get narrower (and the peak values greater) as the correlation between the model velocities at the two altitude levels increases. When the correlation is equal to 1 (i.e., the model velocities are equal at both altitudes), then the flux is identically equal to zero and its distribution is infinitely narrow. The asymmetry of the distribution increases as the time lag between the model velocities increases.

The distribution of the seismic flux values derived from the observations is displayed as the solid curve in Figure 1. The distributions of seismic flux in two models are displayed as the dotted and dashed curves. The dotted curve represents a model that was chosen such that its values fit the slopes of the observational distribution at small positive and negative flux values. It was generated with a correlation coefficient of 0.9993 and a time lag (of the top altitude relative to the bottom altitude) of $+0.37$ s. The dashed curve represents the model that has no time lag (i.e., is symmetric around zero flux) and whose slope fits the slope of the observational distribution at small negative flux values. It was generated with a correlation coefficient of 0.9996.

The observed distribution is qualitatively similar to the model distributions, but it shows enhanced number frequencies (and scale fluxes) at high flux magnitudes, which none of the models show. The observed distribution is also asymmetric, even though the data have been reduced to a common time base (§ 3.1). We ascribe both the enhancement at high flux magnitudes and the distribution asymmetry to seismic events, which were not explicitly included in the models.

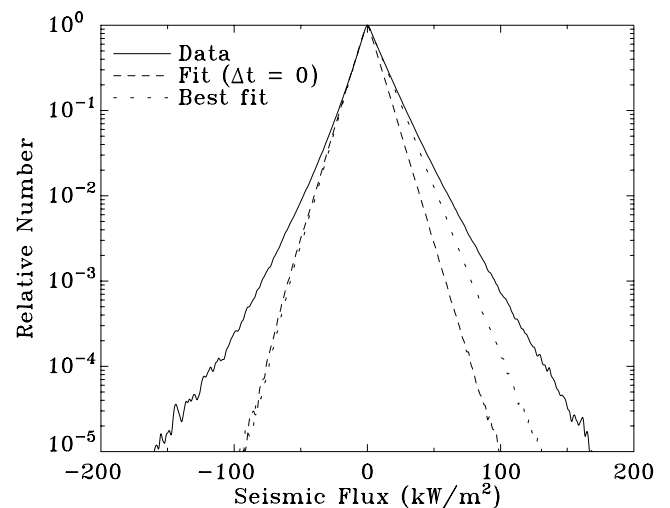


FIG. 1.—Smoothed relative number frequency vs. seismic flux. *Solid curve*: observations; *dotted curve*: the model that fits best at small positive and negative flux values; *dashed curve*: the model with zero time lag that fits best at small negative flux values.

For the symmetric model, the model number frequencies exceed the observational number frequencies by a factor of 2 or more for fluxes more negative than -41 kW m^{-2} or more positive than $+20 \text{ kW m}^{-2}$.

6. SEISMIC EVENTS

Rimmele et al. (1995a) observed that the quiet Sun is peppered with seismic outbursts that burst forth from the dark intergranular lanes. They showed that a typical outburst is preceded by an abrupt darkening of the lane and argued that they were seeing the surface effects of seismic events that excite solar oscillations immediately beneath the photosphere. We build on the work of Rimmele et al. (1995a, 1995b) and Goode et al. (1998) by superposing, and aligning in space and time, the evolution of hundreds of seismic events in the photosphere.

6.1. Seismic Event Identification

We located seismic events as follows: First, we smoothed the seismic flux values, using a spatial gaussian filter with a FWHM of 3 pixels (0.4 Mm, 0.6), to reduce fragmentation in the final results due to noise. Then, we applied a three-dimensional data segmentation algorithm to the smoothed seismic flux data cube. Finally, we applied a threshold to select only the most significant segments. Because we apply the threshold *after* detection, the extent of accepted segments does not depend on the threshold.

The segmentation involves determination for each data element if the data show negative curvature (i.e., a central value exceeding the average of the two adjoining values on opposite sides) in all thirteen directions through the center of a data cube of 3 by 3 by 3 elements centered on the data element under consideration. Only data points meeting this criterion are considered to be part of some segment.

Individual segments were identified in the three-dimensional data cube by demanding that (1) all data points in a particular uniquely identified segment are linked through nearest-neighbor connections and that (2) all data points in a particular segment are connected, through steepest-ascent paths, to the same local maximum. In this way, 27,247 segments were detected, covering 9.2% of the whole data volume. We then excluded those segments that

did not contain a local maximum in the unsmoothed seismic flux, leaving 16,839 seismic events that collectively cover 8.2% of the data volume. We refer to the location and time of the local maximum associated with each seismic event as its *central location and time*.

Because at this stage no data-set-specific threshold has yet been applied, noise artifacts likely exist among the detected events. We employ suitable thresholds where necessary.

Figure 2a displays the fractional area coverage of seismic segments with maximum seismic flux exceeding some lower limit F_0 , as a function of F_0 . For F_0 between about 50 and 160 kW m^{-2} , the curve is approximated well by $A(F_0) = 0.25 \exp[-F_0/(23 \text{ kW m}^{-2})]$ (indicated in the plot). Figure 2b similarly displays the birth rate of seismic events as a function of lower flux limit F_0 . For F_0 between about 50 and 160 kW m^{-2} , the curve is approximated well by $B(F_0) = 5.2 \times 10^{-15} \exp[-F_0/(20.9 \text{ kW m}^{-2})] \text{ m}^{-2} \text{ s}^{-1}$ (indicated in the plot).

6.2. Measuring the Average Seismic Event

The temporal and spatial evolution of any particular quantity of the “average” seismic event was determined by averaging the desired quantity as a function of time and horizontal position relative to the central location and time of each seismic event.

To gather useful directional information, we determined the local spatial orientation of the structures (read: intergranular lanes) in the continuum intensity at the time and position of the largest seismic flux value in each seismic event, using the inertia tensor method (Jähne 1993), such that rotation of the continuum images around the central position through the found orientation angle lines the local structure (lane) up with the x axis. We resolved the 180° ambiguity in the rotation angle by demanding that the brightest continuum structure near the central position be placed at $y < 0$. We used the same angle to rotate the images showing the desired quantity around the central position, and then averaged over all events. This process of determining averages is referred to in this paper as *centering*. All of our results were centered in a data volume of 7.8 Mm by 7.8 Mm by 21 minutes. Only those seismic events were included that were sufficiently far from the edges of the

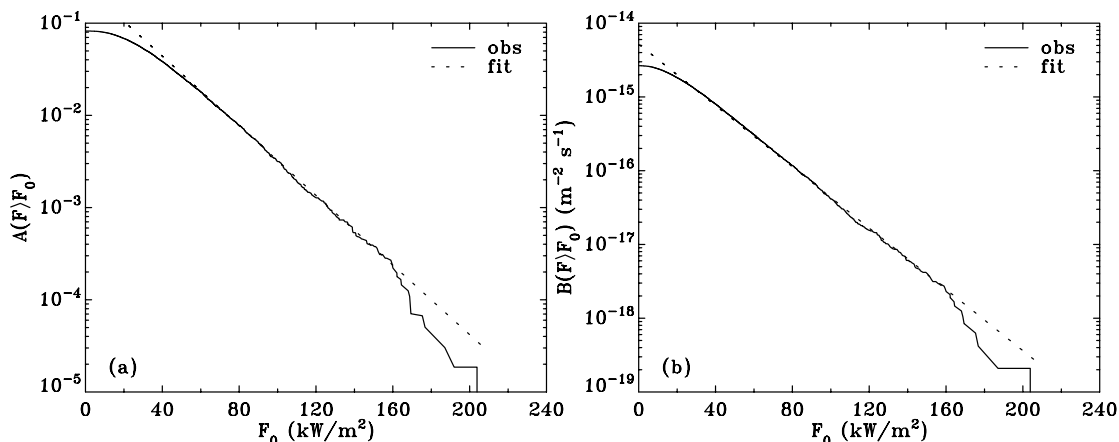


FIG. 2.—Covered fraction $A(F > F_0)$ of the surface area (a) and the birth rate $B(F > F_0)$ (b) of seismic segments of maximum seismic flux F greater than F_0 , as a function of F_0 . Exponential fits (determined by eye) are indicated by the dotted lines.

data volume to yield data at each time and position in the centered average.

6.3. Characteristics of the Average Seismic Event

6.3.1. Systematic Components

Because the rotation angles used in centering are based on continuum intensity, we find systematic results for centered continuum intensity even when we pick random positions and times and use them for central positions and times of “events” that we will refer to as *fake events*. Figure 3 compares centered continuum intensity associated with the seismic events and the intensity associated with a similar number of fake events. Each panel shows average continuum intensity per included seismic event. In each case, only the events with maximum seismic flux at least as great as a threshold F_0 were included. The threshold F_0 decreases from 75 kW m^{-2} in the left column to 20 kW m^{-2} in the

right column, and the number of included events increases from about 400 at the left to about 5000 at the right.

The top row shows the results for the seismic events, which become somewhat less distinct as the seismic flux threshold F_0 decreases from panel *a* to panel *c*. There is a bright roundish structure at $y < 0$, a larger bean-shaped dark structure near $y = 0$, and a barlike dark structure along $x = 0$ in the direction of positive y . Are these structures associated with the seismic events, or are they related to the data reduction? The used algorithm prefers something bright at $y < 0$ and something dark at $y > 0$ (§ 6.2), so it is not surprising if we find such structures there.

The middle row of Figure 3 shows results that are based on random positions and times, so they have no particular preference for seismic events. These results remain the same, on average, regardless of the number of included fake events, and show essentially the same structures as the reduced observations in the top row of Figure 3. This indi-

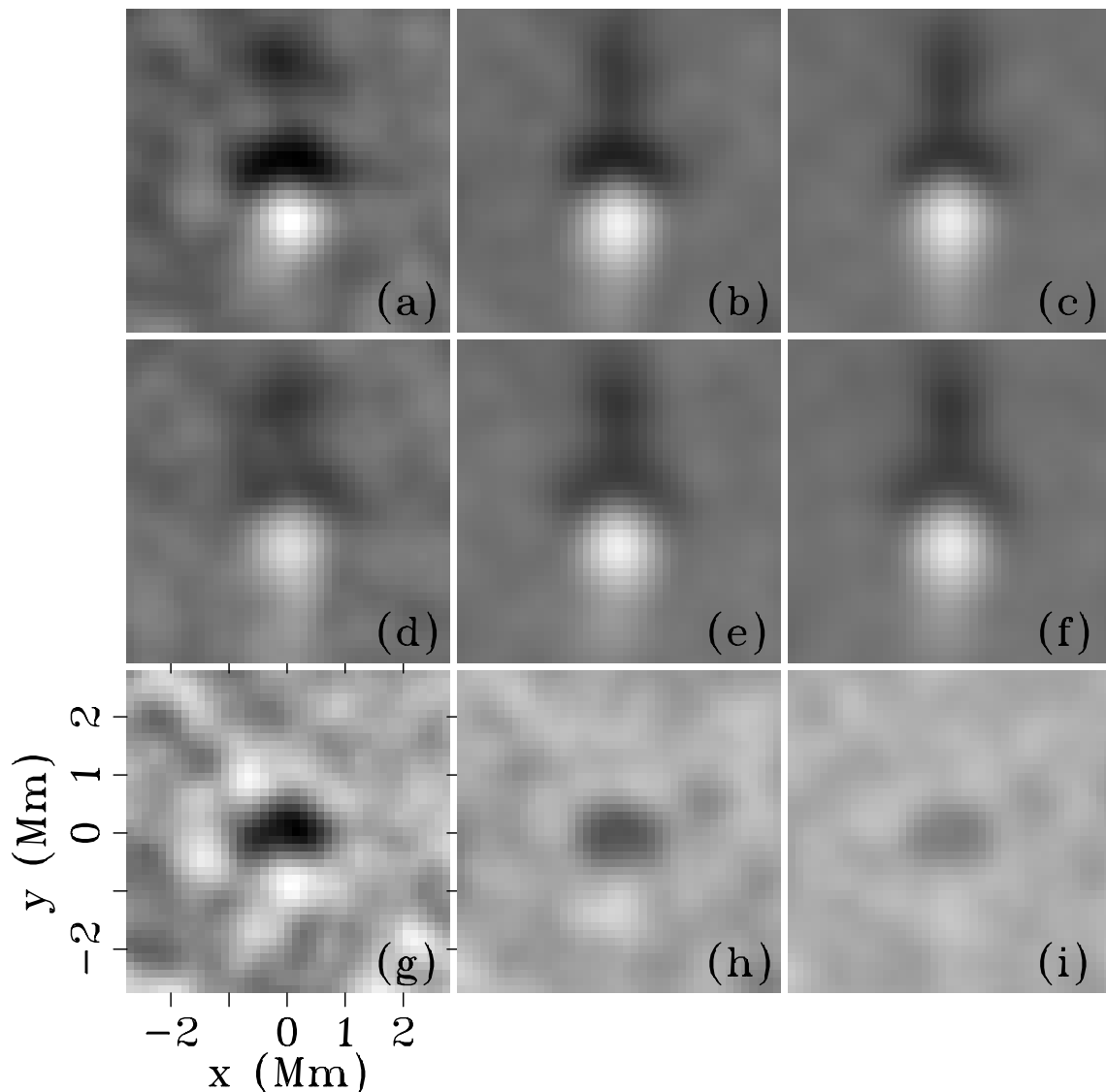


FIG. 3.—Centered continuum intensity. *Top row (a, b, c)*: results based on seismic events. *Middle row (d, e, f)*: results based on random positions and times. *Bottom row (g, h, i)*: difference between seismic and random results. *Left column (a, d, g)*: events with $F_0 > 75 \text{ kW m}^{-2}$. *Middle column (b, e, h)*: $F_0 > 40 \text{ kW m}^{-2}$. *Right column (c, f, i)*: $F_0 > 20 \text{ kW m}^{-2}$. Contrast limits of top and middle rows: 0.984–1.024 times the average continuum; of bottom row: -0.014 to $+0.006$ times the average continuum.

icates that most of what is visible in the reduced observations is not associated with the seismic events but rather associated with the reduction method, and that correction of the results is necessary if we want to detect the influence of the seismic events.

The difference between the top and middle rows is due to the seismic events alone, and this is displayed in the bottom row of Figure 3. We refer to it as the *residual continuum intensity*.

The results (not displayed) for the convective Doppler velocity look very much like those for the continuum. The centered seismic flux of fake events shows no systematic variation with space or time.

6.3.2. Significant Events

Figures 3g–3i show that the amplitude of the residual continuum intensity decreases as the lower threshold F_0 on the maximum seismic flux of the events decreases, but that the spatial pattern remains essentially the same, which means that the spatial pattern is systematic rather than random. Figure 4 displays the magnitude of the minimum residual continuum intensity as a function of the number N of included events (in descending order of maximum seismic flux). At any given position (and in particular at the position of the minimum) the average residual continuum intensity of the first N events is equal to $I_{\text{avg}}(N) = \sum_{k=1}^N I_k / N$. If $I_k \sim k^\alpha$ for $k \leq N_0$ and $I_k = 0$ for $k > N_0$, then $I_{\text{avg}}(N) \sim N^\alpha$ for $N \leq N_0$ and $I_{\text{avg}}(N) \sim N^{-1}$ for $N > N_0$. The magnitude of the minimum residual continuum intensity shows a power-law dependence on N for $N < 2000$ ($F_0 > 40 \text{ kW m}^{-2}$) with $\alpha \approx -0.33$, so all of those events contribute to the continuum. For $N > 5000$ ($F_0 < 20 \text{ kW m}^{-2}$) the curve tends toward $\alpha = -1$ (an appropriate fit is shown) so those events do not appear to contribute to the continuum. We adopt $F_0 = 40 \text{ kW m}^{-2}$ as a lower threshold for significant seismic events. It is not clear if this lower threshold reflects the physics of seismic events or rather some observational limit.

6.3.3. Slices

Two slices each through the average residual continuum, residual convective velocity, and seismic flux data are dis-

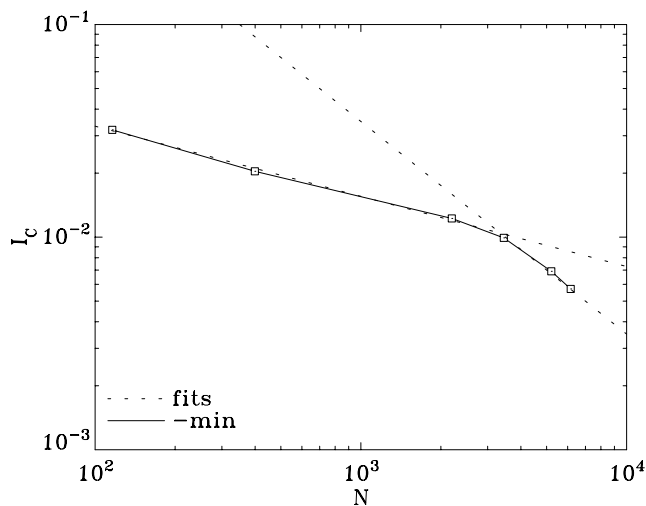


FIG. 4.—Normalized magnitudes of the minimum centered residual continuum intensity I_c vs. the number N of included seismic events (in descending order of maximum seismic flux). Boxes connected through the solid curve: observational data. Dotted lines: power-law fits.

played in Figure 5. These are equal to the difference between the average quantities derived from 2199 seismic events with $F_0 > 40 \text{ kW m}^{-2}$ and the average quantities derived from fake events at random positions and times, as described in § 6.3.1. These panels show the difference that the presence of seismic events makes, *not* (for the continuum and Doppler velocity) their average appearance. For the average appearance of the events in the continuum, see Figure 3.

Figure 5 shows that the seismic events are associated with prior residual continuum darkening and downflows, centered on $(x, y) = (0, 0)$. The average residual continuum darkening reaches 0.012 times the average continuum, peaks at about $t = -3.5$ minutes, and has a FWHM duration of 10.1 minutes and size (at $t = -3$ minutes) of 1.0 Mm (according to least-squares Gaussian fits). The residual downflow reaches 30 m s^{-1} , peaks at $t = -3.2$ minutes, and has a FWHM duration of 12.4 minutes and size (at $t = -3$ minutes) of 0.94 Mm.

It is likely that the locations of the maximum effect of a given seismic event on the continuum intensity and Doppler velocity do not coincide exactly with the location of the maximum seismic flux. Variations in the properties of the medium, to which the different measurements are unequally sensitive, lead to inherent differences, and the nonlinear nature of the seismic flux leads to variation in the location of the maximum seismic flux depending on the phases of the local p -modes. This means that the small values of the spatial maximum of the average continuum darkening and downflow may underestimate the “typical” maximum in any given event.

The seismic flux shows, by construction, a peak at (0,0,0). The peak value is 60.3 kW m^{-2} , and the peak has a FWHM duration of 3.6 minutes and size (at $t = 0$) of 0.6 Mm. The temporal evolution of the seismic flux is discussed further in § 6.3.4.

Figure 6 shows the dependence of various measures of the magnitude of the centered seismic event on the seismic flux threshold. The magnitudes of the seismic events in continuum and Doppler velocity are considerably smaller than the typical amplitude of granulation in the same quantities (as indicated by the standard deviations) so individual seismic events cannot readily be identified in continuum or Doppler velocity data. Inspection of a number of the individual aligned images that go into the average shows that individual examples do not often resemble Figure 5 in detail; there is much variation around the average from instance to instance. The small amplitudes also indicate that though the seismic events are associated with continuum darkening, they are by no means confined to the very centers of the darkest intergranular lanes. Visual inspection of a number of individual events shows that some of them even occur in the middle of granules, but in those cases the granule center is generally failing, i.e., darkening.

Figure 7a displays the total seismic energy per event, versus seismic flux threshold F_0 , for positive (upgoing) and negative (downgoing) flux separately. We corrected for two sources of systematic bias. The first source of bias is that the average seismic flux outside of seismic events is not zero, because of the nonlinear nature of seismic flux as a function of velocity (§ 5), so we subtracted the spatial-temporal average of the centered model seismic flux from the observational and model seismic fluxes before calculating the total energies for both flux signs. The second source of bias

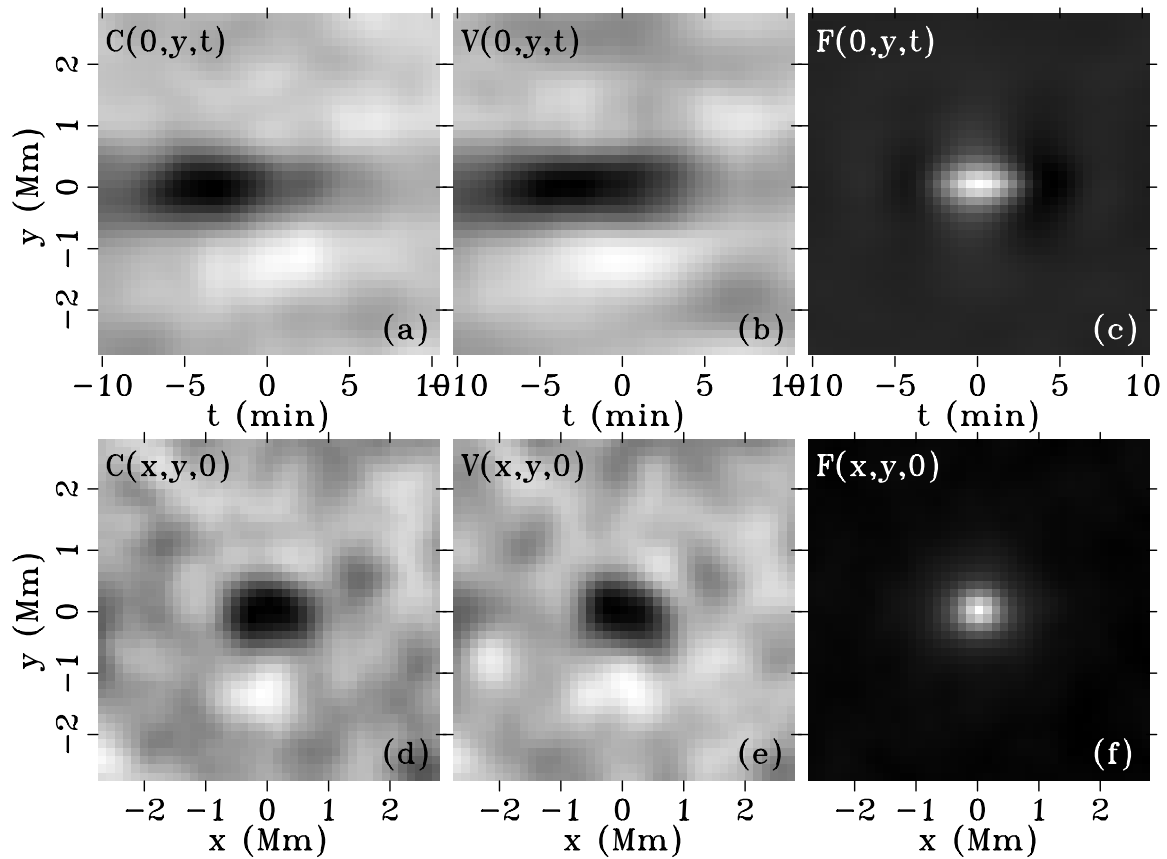


FIG. 5.—Centered residual continuum intensity (*a* and *d*), convective Doppler velocity (*b* and *e*), and seismic flux (*c* and *f*). Each panel shows the difference between the results for the seismic events and the corresponding results for a similar number of random positions. Coordinates $(x, y, t) = (0, 0, 0)$ correspond to the time and place of maximum seismic flux. The top three panels show quantities at $x = 0$, and the bottom three at $t = 0$. The gray scales runs between the following limits: *a*: -0.012 through $+0.003$ average continua; *b*: -31 through $+21$ m s^{-1} ; *c*: -9 through $+57$ kW m^{-2} ; *d*: -0.007 through $+0.003$ average continua; *e*: -27 through $+20$ m s^{-1} ; *f*: -1 through $+57$ kW m^{-2} .

is that sums of magnitudes are not zero even when the signed average is, so we subtracted the totals for the model flux (labeled “Offset” in Figure 7*a*) from the absolute totals for the observational flux, and the results are referred to as the systematic positive and negative energies.

For $F_0 \leq 75 \text{ kW m}^{-2}$, the systematic positive energy varies roughly as $1.35 \times 10^{19} [F_0/(40 \text{ kW m}^{-2})]^{5/4} \text{ J}$, and the systematic negative energy is fairly constant, at $2.7 \times 10^{18} \text{ J}$. When we combine these systematic energies with the seismic event birth rates from Figure 2*b*, then we

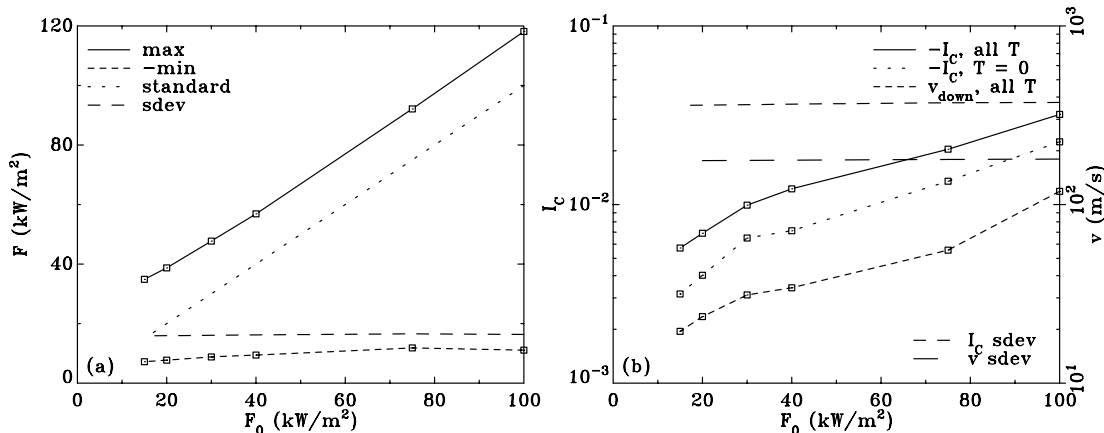


FIG. 6.—Centered seismic event properties vs. lower threshold F_0 on the maximum seismic flux per event. (*a*) The maximum seismic flux (solid curve), negative of the minimum seismic flux (medium-dashed curve), $F = F_0$ (dotted curve), and standard deviation of nonevent flux (long-dashed curve). (*b*) The maximum residual continuum darkening in units of the average continuum intensity (solid curve), the maximum residual continuum darkening at $T = 0$ only (dotted curve), and the standard deviation of nonevent continuum intensity (medium-dashed curve), all on the left-hand scale, and the maximum residual downward Doppler velocity (short-dashed curve) and standard deviation of nonevent Doppler velocity (long-dashed curve), all on the right-hand scale.

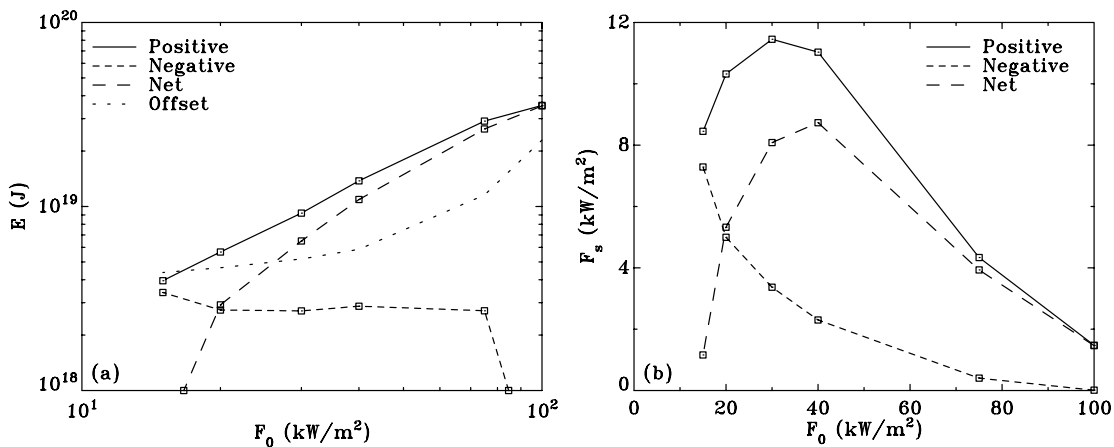


FIG. 7.—(a) Total seismic energy E per seismic event vs. lower threshold F_0 on the maximum seismic flux of the included seismic events. *Solid curve*: systematic positive seismic flux. *Short-dashed curve*: systematic negative flux. *Medium-dashed curve*: systematic net flux. *Dotted curve*: systematic offset. (b) Equivalent systematic seismic flux when spread over the whole solar surface, vs. F_0 .

get the equivalent systematic seismic flux of Figure 7b, the average flux when spread over the whole solar surface. The net equivalent systematic seismic flux is greatest, at about 8.7 kW m^{-2} , for a flux threshold of about 40 kW m^{-2} —i.e., the threshold we established in § 6.3.2 for significant seismic events.

6.3.4. Temporal Evolution of the Seismic Flux

In Figure 5 the observed seismic flux shows a prominent positive peak without marked spatial anisotropy, preceded and followed by much less prominent dips. The temporal evolution at the position of maximum seismic flux is shown as the solid curve in Figure 8. The best-fitting seismic flux model from § 4 yields the average seismic flux displayed as the medium-dashed curve in Figure 8. The model, which did not include any seismic events, reproduces the preceding flux dip in the observational data but has a much lower peak value and does not reproduce the following flux dip well.

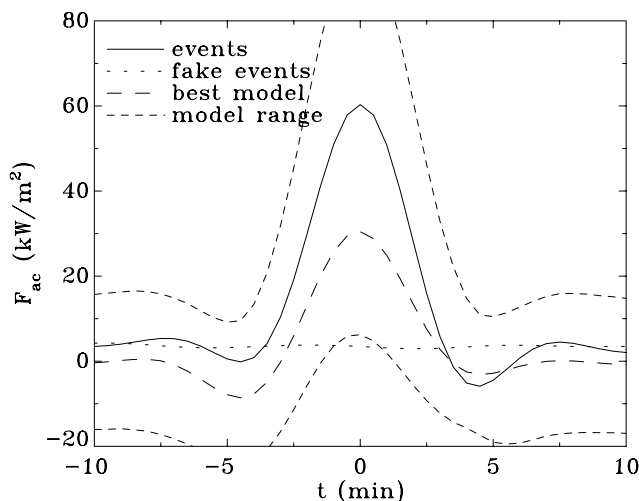


FIG. 8.—Seismic flux at the position of maximum seismic flux, averaged over all seismic events with maximum seismic flux exceeding 40 kW m^{-2} , as a function of time t relative to the time of maximum seismic flux. *Solid curve*: seismic events; *dotted curve*: fake events; *medium dashed curve*: the “best” model from § 5 and Fig. 1; *the two short-dashed curves*: the minimum and maximum over all models from § 5.

Many models, including the best-fitting one displayed in Figure 8, reproduce the shape and amplitude of the dip preceding the peak in the seismic flux derived from the observations. None of these models includes seismic events, so we conclude that the preceding dip can be explained fully as an artifact of the data reduction. It might be related to the temporal filtering we applied to remove the granular signal from the data (§ 3.3).

The two short-dashed curves in Figure 8 indicate the range of seismic fluxes found over all of the investigated models. Within the inspected range of models, the average seismic flux values at $t = -10$ and $t = +10$ minutes depend mainly on the time lag, at about $2.2 \text{ kW m}^{-2} \text{ s}^{-1}$ of time lag, and hardly on the cross-correlation. The maximum flux (at $t = 0$), however, depends markedly on both the time lag (at about $3.7 \text{ kW m}^{-2} \text{ s}^{-1}$) and the cross-correlation (decreasing over about 6.4 kW m^{-2} when the correlation rises from 0.997 to 1.000). One can therefore, by suitably decreasing the cross-correlation, find models that show nearly the same peak amplitude as the observations do. However, such models yield peaks that are too wide to fit the observed peak and do not fit the observed flux histogram (Fig. 1) as well as the best-fitting model does, which has a lower peak value.

None of the models fits the following dip. In particular, none of them reproduces the observation that the following dip is deeper than the preceding one. We ascribe the following dip to the seismic events.

We conclude that the preceding dip is an artifact, but that the peak and following dip are significant: within a few minutes after the passage of seismic waves traveling up, some seismic waves traveling down are observed. We interpret these as due to the reflection of some of the flux that was traveling upward.

We cannot tell from the current observations exactly what the temporal profile of the downward reflected flux is, or when its greatest value is attained, because a significant part of it may be obscured by the tail end of the upward traveling flux. Because of the nonlinear nature of the dependence of seismic flux on the velocities we cannot predict what the shape of the seismic flux profile (vs. time) of an upward seismic impulse should be, or even if it should be symmetric, so we cannot disentangle the partially overlap-

TABLE 1
LEAST-SQUARES FITS TO THE SEISMIC FLUX PROFILE

Model	b	A_1	t_1	w_1	A_2	w_2	A_3	t_3	w_3	σ
I.....	4.0(6)	6(2)	-4.0(5)	2.5(9)	57(2)	4.0(1)	12(2)	+4.1(3)	2.9(5)	0.6
II.....	2.7(3)	8.7(8)	-2.4(2)	3.9(4)	63.5(7)	4.51(5)	12.5(7)	+3.2(2)	4.5(3)	0.3

NOTE—Model I: Three Gaussians. Model II: Gaussian+sinc²+Gaussian. The three components are indicated by subscripts 1, 2, and 3. The b is the seismic flux offset in kW m⁻², A the magnitude of the amplitude in kW m⁻², t the central time in minutes relative to the peak, w the FWHM in minutes, and σ the average residual error in kW m⁻². Numbers in parentheses indicate the formal error in units of the last digit of the preceding value.

ping upward and downward fluxes. However, we may get some indication by fitting likely functions to the profile. Table 1 lists the parameters from two least-squares fits to the data, modeling the preceding and following dips with Gaussians and the central peak with a Gaussian (model I)

or a sinc² function (model II). Models with fewer components yield significantly worse fits. The results indicate that the fits are very good and suggest that the downward reflection may be centered as little as 3.2 minutes after the peak in the upward flux.

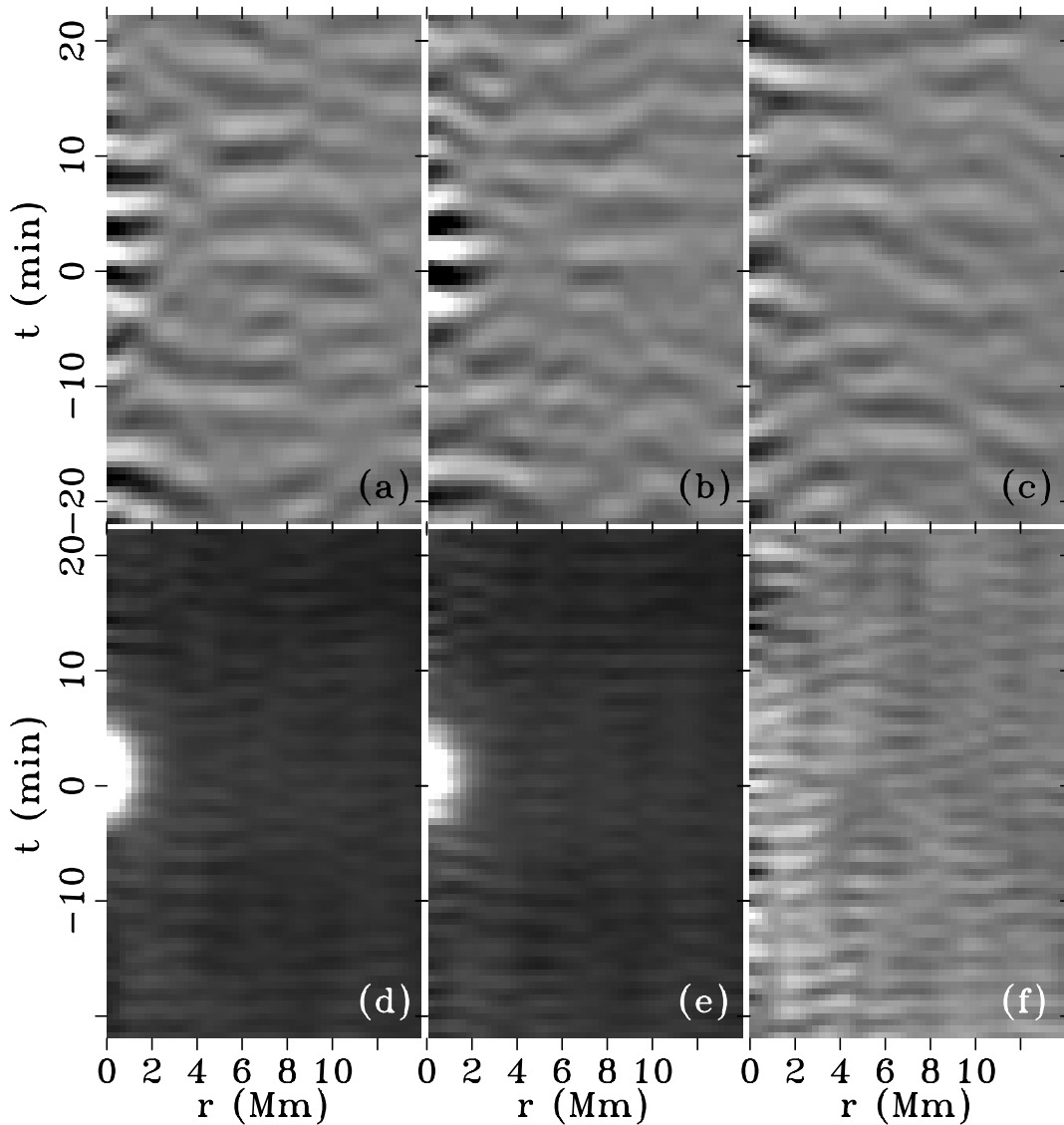


FIG. 9.—Ripple diagrams of the sonic speed of the seismic events exceeding a maximum seismic flux of 100 kW m⁻², as a function of spatial distance r and temporal distance t to the centers of the events. The top row (panels a, b, c) shows the average, the bottom row (d, e, f) the standard deviation of the speed distributions. The left column (a, d) shows results for the positions and times of the seismic events; the middle column (b, e) shows results for positions and times of the convective downdraft nearest the position of maximum seismic flux in each event; and the right column (c, f) shows results for random downdrafts. The number of events that contribute to each displayed value varies between 149 and 254, and the number of velocity data values between 149 and 101,357. The displayed contrast ranges between -37 and $+37$ m s⁻¹ in panels a, b, c , between 203 and 364 m s⁻¹ in panels d, e , and between 203 and 260 m s⁻¹ in panel f .

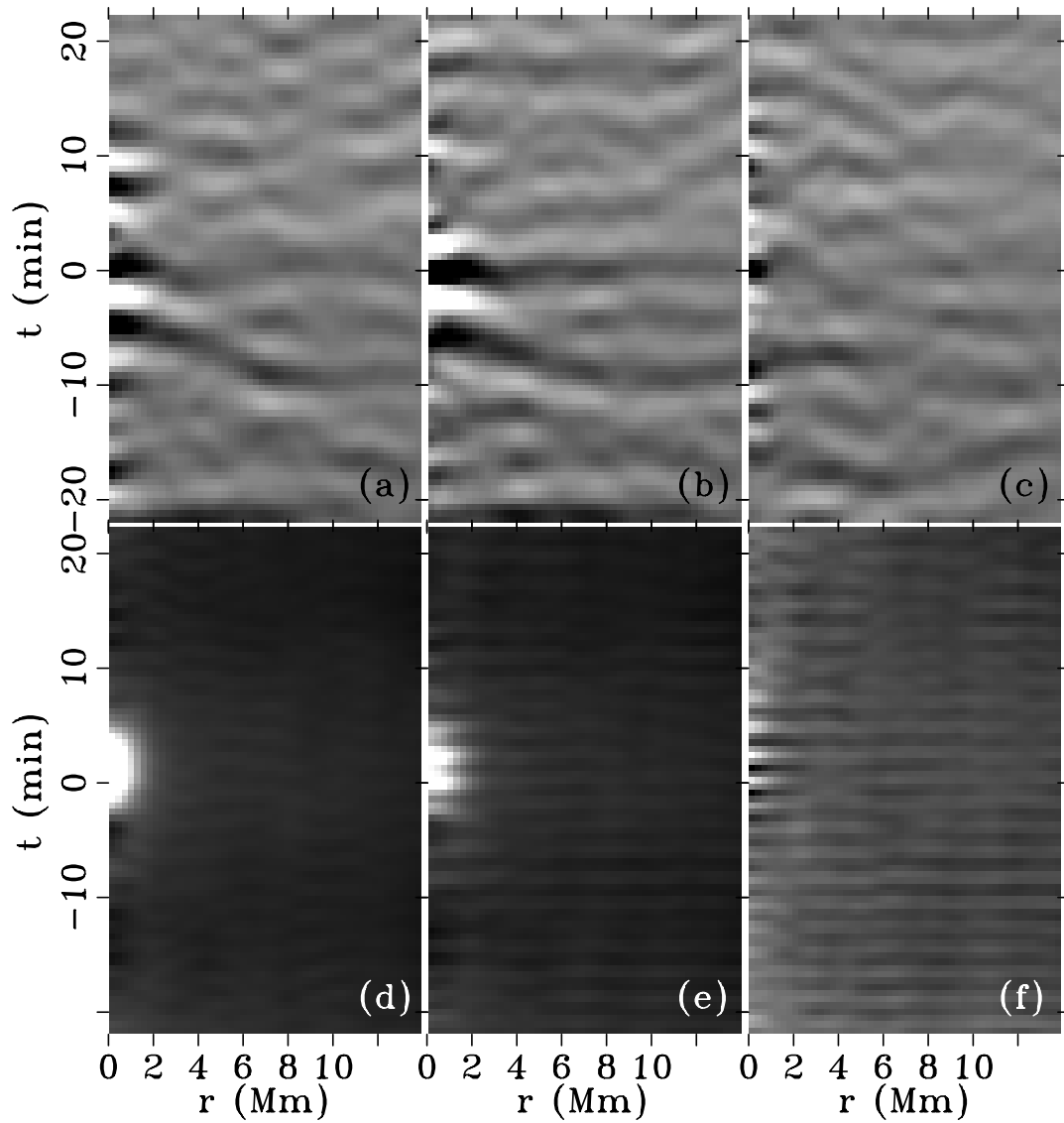


FIG. 10.—Same as Fig. 9, but for seismic events exceeding a maximum seismic flux of 40 kW m^{-2} . The number of events that contribute to each displayed value varies between 2861 and 4455, and the number of velocity data values between 2861 and 1,766,766. The displayed contrast ranges between -10 and $+10 \text{ m s}^{-1}$ in panels *a*, *b*, *c*, between 222 and 306 m s^{-1} in panels *d*, *e*, and between 222 and 255 m s^{-1} in panel *f*.

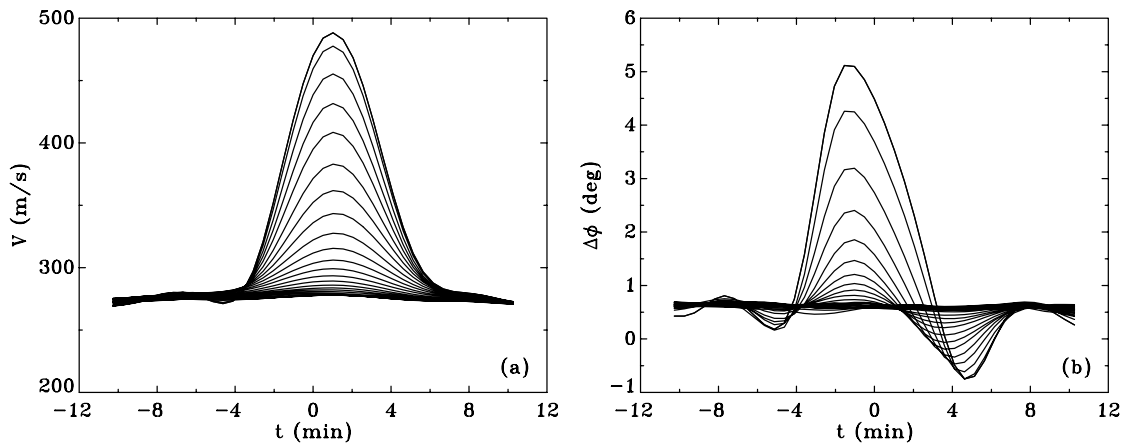


FIG. 11.—Sonic velocity amplitude (*a*) and phase difference (*b*) averaged over all seismic events with $F > 40 \text{ kW m}^{-2}$, as a function of time, for radial distances from 0 through 4.0 Mm in steps of 0.14 Mm (1 px). The curves for $r = 0$ show the greatest amplitude, and the amplitude drops smoothly with increasing distance r .

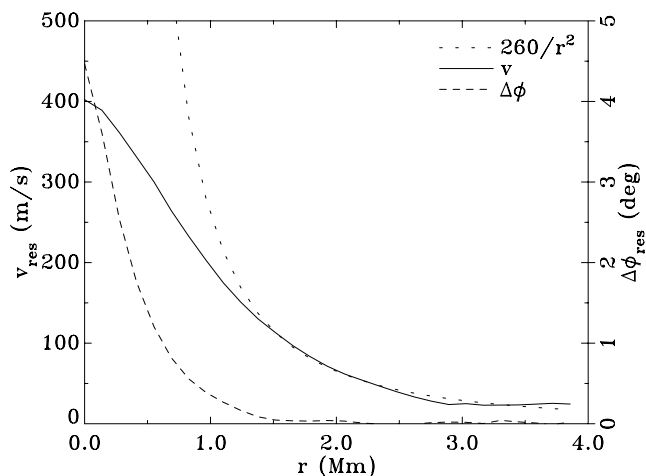


FIG. 12.—Residual seismic event velocity amplitude vs. distance to the epicenter (solid curve, left-hand scale), a r^{-2} fit (dotted curve, left-hand scale), and the residual phase difference (dashed curve, right-hand scale).

6.4. Ripple Diagrams

Because seismic events are localized sources of wave energy, one might expect to see disturbances traveling radially outward from the sites of seismic events. We study this by aligning all seismic events on their central position and studying the velocities as a function of radial distance to the center of the events and of time relative to the time of the event maximum. We refer to the resulting two-dimensional images of velocity versus distance and time as *ripple diagrams*, because one might detect radially traveling ripples in them.

Figures 9 and 10 show ripple diagrams of the sonic speed for seismic events whose maximum seismic flux exceeds 100 (Fig. 9) and 40 kW m^{-2} (Fig. 10), respectively, for three different selections of times and positions: the times and positions of maximum seismic flux in seismic events (left

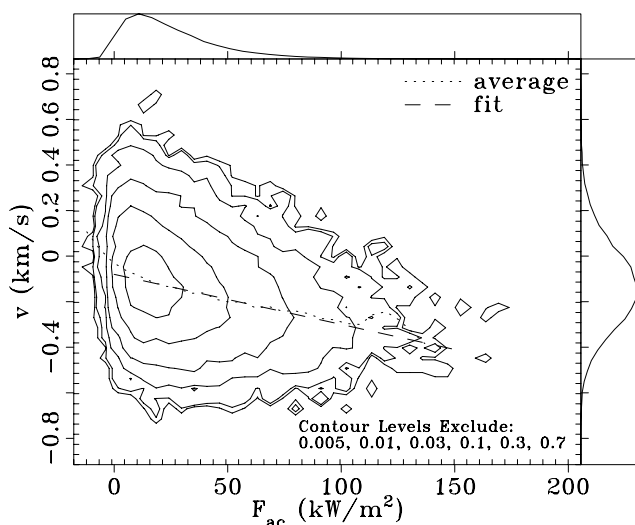


FIG. 13.—Contour plot of the number frequency distribution of the largest downward velocity (with up counted positive) versus the maximum seismic flux in all seismic segments. The contour levels indicate the fraction of data points that lies on the outside of the corresponding contour. For instance, the central contour includes 30% of data points. *Side panels*: the associated one-dimensional distributions. *Dotted curve*: the average velocity for given flux levels. *Dashed line*: a fit to the dotted curve.

column), the times and places of maximum convective downdraft reached from the times and places of maximum seismic flux by walking along the steepest velocity gradient (*middle column*), and a set of randomly selected convective downdrafts (*right column*). We include the middle column because the nonlinear dependence of seismic flux on velocity (§ 3.3) may cause the position of the maximum seismic flux to be influenced by unrelated p -modes in the same area. The position of the nearest local downdraft is presumably not similarly affected.

The two figures are quite similar. All panels in both figures point to a periodicity in the data of about 5 minutes, which is to be expected since the shorter-period convective velocities were filtered out. The seismic events are reflected in an enhancement of the standard deviations for $r < 3$ Mm and $|\Delta t| < 5$ minutes in the left two columns. At $r > 3$ Mm, the statistical characteristics of all three selections are very similar. Coherent ripples of sufficient magnitude would show up in the average velocities (panels *a* and *b*) though perhaps not in the standard deviations (panels *d* and *e*), and incoherent ripples would enhance the standard deviation though perhaps not the average. We see no significant enhancement in either the average or the standard deviation at $r > 3$ Mm. The rms variation in the average velocity at $r > 3$ Mm is about 5 m s^{-1} for $F_0 > 100 \text{ kW m}^{-2}$ (Fig. 9) and about 2 m s^{-1} for $F_0 > 20 \text{ kW m}^{-2}$ (Fig. 10). We conclude that there are no ripples with amplitudes greater than about 1 m s^{-1} associated with seismic events in the current data set.

The average sonic velocities, of the order of 30 m s^{-1} or less, are much smaller than the sonic velocity standard deviations, which are of the order of 270 m s^{-1} . This indicates that there is not much correlation, if any, between seismic events and the phase of velocities in the p -mode region of the k - ω diagram at the same locations. We conclude that the seismic events are not triggered by (constructive interference of) p -modes.

6.5. Average Power and Phase

Figure 11 shows the velocity power (panel *a*) and phase difference (panel *b*) averaged over all seismic events exceeding 40 kW m^{-2} , as a function of temporal (t) and spatial (r) distance from the center of the seismic events. The phase difference at great $|t|$ is not equal to zero, which is consistent with the asymmetry of the seismic flux distribution (Fig. 1). The phase difference at $r = 0$ reaches a maximum of 5.2 degrees at $t = -1.3$ minutes. The velocity amplitude reaches a maximum of 489 m s^{-1} at $t = +1.0$ minutes. The difference between the peak times for the velocity amplitude and phase difference is likely related to the evanescent character of the vertically traveling waves in the p -mode region.

We established before that the seismic events have no particular correlation with the phases of the local p -modes, so the seismic event velocities and the p -mode velocities add incoherently, and the square of the amplitude of the total velocity equals the sum of the squares of the amplitudes of the p -mode and event velocities. Figure 12 displays the maximum residual (event) velocity amplitude over all t , versus distance r from the event center, assuming a value of 277 m s^{-1} for the p -mode velocity amplitude, and also the residual phase difference (i.e., after subtraction of an offset so that it ends up near 0 for large r). The residual phase difference drops much faster than the velocity amplitude does when r increases. For $r \geq 1.5$ Mm, the residual phase

difference is essentially zero, but the residual velocity amplitude is approximated reasonably well by $260/r^2$ in meters per second, with r in Mm. We conclude that the upward traveling waves are partly converted into horizontal waves. However, the r^{-2} behavior of the velocity amplitude for $r \geq 1.5$ kW m⁻² does not fit either far-field spherical waves (which have r^{-1} dependence) or cylindrical waves ($r^{-1/2}$).

7. DOWNWARD VELOCITY VERSUS SEISMIC FLUX

Figure 13 displays the frequency distribution of the greatest downward velocity anywhere in each seismic segment versus the greatest seismic flux in the same segment. There is a roughly linear relationship between the flux amount F_{ac} and the velocity v (measured positive upward), as indicated by the correlation coefficient of -0.31 (highly significantly different from zero; 95% confidence limit: 0.015) and expressed by the fit formula

$$\frac{v}{\text{m s}^{-1}} = -2.2 \frac{F_{ac}}{\text{kW m}^{-2}} - 80, \quad (9)$$

which is indicated by the dashed line in Figure 13.

Lighthill (1952) predicted that the intensity of acoustic waves should be proportional to the eighth power of the convective velocity, assuming that p -modes are formed through turbulent excitation. We see no evidence of such a high power in our data.

8. CONCLUSIONS AND DISCUSSION

We studied the properties of temporally and spatially isolated occurrences of generation of wave energy below the solar surface (“sunquakes”) in the p -mode region of the k - ω diagram. The photospheric (surface) aspects of these energy generation bursts, seismic events, are detected in seismic flux, a proxy for vertical wave energy flux based on measurement of line profiles (§ 3.3). The seismic events form a distribution whose properties we studied as a function of the lower threshold F_0 on the maximum seismic flux F in each event. The events with $F \geq 40$ kW m⁻² form a fairly consistent set; below that limit the area coverage and birth rate level off (Fig. 2) and the bulk of the events do not contribute to the continuum (Fig. 4) and surface-wide seismic flux balance (Fig. 7). We call events above this threshold *significant seismic events*. Below, we describe the characteristics of the significant seismic events. For information on how these vary with F_0 , see the main text.

We determined the average properties of the seismic events after aligning them all to their time and location of greatest seismic flux, aligning them with the local continuum structure along the x -axis (§ 6.2), and subtracting systematic components not explicitly related to the seismic events (§ 6.3.1). The average significant event consists of (Fig. 5):

1. A residual darkening in the continuum intensity. Averaged over all significant events, the residual darkening reaches at most 0.012 of the average continuum. It lasts about 10 minutes (FWHM), peaks at $t = -3.5$ minutes and then has a FWHM diameter of 1.0 Mm.

2. A photospheric residual downflow with an amplitude of about 30 m s⁻¹, lasting about 12 minutes, peaking at $t = -3.2$ minutes and 0.9 Mm.

3. Seismic flux. The flux profile shows strong upward flux at $t = 0$ (by definition), peaking at 60 kW m⁻², lasting about 3.6 minutes, and reaching 0.6 Mm in FWHM size.

Part of the upward seismic flux is reflected down again and shows up in downward flux following the upward peak. The downward flux is centered at about $t = +3$ minutes, has an amplitude of about 12 kW m⁻², and lasts 3–5 minutes. There is also a preceding dip, centered at about $t = -3$ minutes, with an amplitude of about 7 kW m⁻² and lasting 3–4 minutes, but we have determined this flux to be an artifact of the data processing (§ 6.3.4).

The found amplitudes of the average residual continuum darkening and residual downflow probably underestimate the average of the amplitudes (§ 6.3.3).

The significant events cover about 4% of the data volume. Their birth rate is about 8×10^{-16} m⁻² s⁻¹, which corresponds to about 5000 new events per second over the whole solar surface (if such extrapolation is warranted). The seismic events yield phase differences between the waves at different altitudes, and a temporary increase in the velocity power. The peak in the phase difference occurs about 2 minutes before the peak in the velocity power (Fig. 11).

This surface display originates in the convection zone. Goode et al. (1992) showed that the seismic events must be excited less than 200 km below the photosphere. Part of the energy generated in such events travels up to the surface for us to detect, and part must travel down. Kumar (1993) showed theoretically that white noise generated in the solar convection zone gradually converts into resonant p -modes after a few refractions, so the presence of seismic events at the surface indicates that power is being fed into p -modes. For a p -mode at $l = 500$ and $\nu = 3$ mHz (i.e., near the peak power in the k - ω diagram), the surface skip distance is about 18 Mm (W. A. Dziembowski 1997, private communication), about a third of the size of our field of view, so we cannot see any direct evidence of future p -modes at the surface within a few Mm from the seismic events.

In the average significant seismic event, the vertical phase difference decays faster with distance from the epicenter than does the wave velocity power (Figs. 11, 12), and between about 1.5 and 2.5 Mm from the epicenter there is still appreciable wave velocity power but no longer any vertical phase difference. This is consistent with the waves having transformed from vertically to horizontally traveling, yet we do not detect any ripples traveling away from the epicenter of the events, down to the resolution limit of about 1 m s⁻¹ at more than 3 Mm from the center (§ 6.4), and the observed $1/r^2$ behavior of the seismic event velocity amplitude at distances between 1.5 and 2.5 Mm from the epicenter does not fit traveling spherical or circular waves.

What triggers seismic events? We find no correlation between the occurrence of a seismic event and the phases of the p -modes in the same period and area, so seismic events are not triggered (nonlinearly) by appropriate constructive interference of p -modes. A continuum darkening and convective downflow precede the upward seismic flux by several minutes, so the events are instigated at the surface, as is granulation (Rast 1995). Based on visual inspection of several cases, Rimmele et al. (1995b) implicate occasional catastrophic cooling and collapse of the solar surface in triggering the seismic events, and our conclusions (based on the same data set) are consistent with this.

The two-dimensional numerical simulations of Rast (1999) show localized cooling at the surface causing acoustic emissions of various types. The localized cooling yields

monopolar acoustic emission, expected to last about 1 minute. The subsequent buoyant (downward) acceleration of the cool material yields dipolar emission for a few minutes. Reynolds stresses associated with the mostly horizontal inflows that balance the descending material yield quadrupolar emission, which dominates after the first few minutes. Our observations show the peak upward seismic flux 3.5 minutes after the associated peak continuum darkening. If one assumes that the peak continuum darkening marks the onset of the cooling-induced downflow, then our observations suggest that for our seismic flux the dipolar and quadrupolar emission sources are the most important.

Goldreich & Kumar (1990) argued for stochastic excitation of p -modes by turbulent convection, which leads to a highly nonlinear dependence of the acoustic power on the turbulent velocity. We find that the magnitude of the peak seismic flux increases only linearly with the peak downgoing convective velocity in the dark lane at the site of the event (Fig. 13). If one assumes that the peak downgoing convective velocity is proportional to the turbulent velocity, then our finding is consistent with a monopolar source (Nigam & Kosovichev 1999), which conflicts with the inference of nonmonopolar emission from the comparison of the times of peak upward seismic flux and peak continuum darkening mentioned before. We believe the case for nonmonopolar emission to be stronger than the case for monopolar emission, but this question can only be settled by investigation of the full velocity field throughout the relevant surface layers of the Sun, for example in realistic three-dimensional numerical simulations.

The seismic events contain about 1.5×10^{19} J each. Combining the energy per event with the birth rate, their energy flux is equivalent to a steady 8.5 kW m^{-2} spread over the whole surface. If the characteristics of the events are similar all across the Sun, then the net seismic event power flowing up through the whole photosphere extrapolates to 5×10^{22} W. Libbrecht (1988) made an order-of-magnitude estimate of about W for the power required to

sustain the whole p -mode spectrum, based on the assumption that the p -modes were stochastically excited by turbulent convection. Our estimate for the energy flux in the *surface* aspects of the events is in the same ballpark, though smaller than Libbrecht's. However, our estimate does not include the energy, associated with the event, that was generated below the surface and traveled in directions other than straight up—i.e., the energy that we expect to go into the p -modes. Also, the seismic flux declines with altitude (Stebbins & Goode 1987) so part of the flux traveling up from its generation site was lost and does not show up in our measurements. All in all, our measurements suggest that the (subsurface) seismic events generate enough energy to sustain the whole p -mode spectrum.

We have not been able to demonstrate direct conversion of seismic event power into p -modes, but rather infer such conversion from the presence of seismic events, which are isolated sources of acoustic noise. Conversion of seismic event power into normal modes is likely a gradual process, requiring several refractions and reflections from the surface, of initially downward-traveling acoustic noise generated by the seismic events (Kumar 1993). Our field of view was too small for a decent search for evidence of such skips, and it is not clear to us what kind of velocity amplitude one can expect at the skip locations. If appreciable amplitudes can be expected, then the seismic events could be used to seismically probe the subsurface layers of the Sun, similar to how seismologists extract information about the Earth's subsurface layers from seismograms recorded at various distances to an earthquake. A model of the response at the solar surface to an acoustic point source just below the surface over several skip distances and times would be helpful as a guide for future observations.

This research was supported by National Science Foundation grant ATM-97-14796, NASA grant NAG 5-4919, and NAG 5-3077 (MDI) at Stanford University and Lockheed Martin ATC.

REFERENCES

- Bonaccini, D., & Stauffer, F. 1990, *A&A*, 229, 272
 Bracewell, R. 1965, *The Fourier Transform and its Applications* (New York: McGraw-Hill)
 Chagelishvili, G. D., Tevzadze, A. G., & Goossens, M. 1999, in *Magnetic Fields and Solar Processes*, ed. A. Wilson (ESA SP-448; Noordwijk: ESA), 14
 Goldreich, P., & Kumar, P. 1990, *ApJ*, 363, 694
 Goode, P. R., Gough, D., & Kosovichev, A. G. 1992, *ApJ*, 387, 707
 Goode, P., Strous, L., Rimmele, T., & Stebbins, R. 1998, *ApJ*, 495, L27
 Grossmann-Doerth, U. 1994, *A&A*, 285, 1012
 Jähne, B. 1993, *Digital Image Processing: Concepts, Algorithms, and Scientific Applications* (2d ed.; Berlin: Springer)
 Kučera, A., Balthasar, H., Rybák, J., & Wöhl, H. 1998, *A&A*, 332, 1069
 Kumar, P. 1993, *PASP*, 42, 15
 Kumar, P., & Basu, S. 1999, *ApJ*, 519, 396
 Libbrecht, K. 1988, *ApJ*, 334, 510
 Lighthill, M. 1952, *Proc. Roy. Soc. London*, A211, 564
 Mihalas, B. 1979, Ph.D. thesis, Univ. Colorado
 Nigam, R., & Kosovichev, A. G. 1999, *ApJ*, 514, L53
 Rast, M. P. 1995, *ApJ*, 443, 863
 ———. 1999, *ApJ*, 524, 462
 Rimmele, T. R. 1994, *A&A*, 290, 972
 Rimmele, T. R., Goode, P. R., Harold, E., & Stebbins, R. T. 1995a, *ApJ*, 444, 119
 Rimmele, T. R., Goode, P. R., Strous, L. H., Stebbins, R. T. 1995b, in *Helioseismology; Proc. 4th SOHO Workshop*, ed. J. T. Hoeksema, V. Domingo, B. Fleck, & B. Battrick (ESA SP-376; Noordwijk: ESA), 329
 Rimmele, T., von der Lühe, O., Wiborg, P. H., Widener, A. L., Dunn, R. B., & Spence, G. 1991, *Proc. SPIE*, 1542, 186
 Stebbins, R., & Goode, P. R. 1987, *Sol. Phys.*, 110, 237
 Stebbins, R., & Marmolino, C. 1989, *Sol. Phys.*, 124, 23
 Stein, R. F. 1967, *Sol. Phys.*, 2, 385
 Stein, R. F., & Nordlund, A. 1998, *ApJ*, 499, 914